A Joint Sparsity Approach to Soil Detection Using Expanded Bands of WV-2 Images

Minh Dao, Chiman Kwan, Sergio Bernabé, Antonio J. Plaza, *Fellow, IEEE*, and Krzysztof Koperski

Abstract—Soil can be used as a damage indicator of landslides and flooding, which expose soil from vegetation canopy. It can also be used as an indirect indicator of illegal tunnel digging activity. This letter presents a sparsity-based approach to soil detection using multispectral satellite images, where both original and synthetic bands have been used. Spatial and spectral information has then been jointly used in soil detection. Extensive experiments clearly demonstrated the feasibility of our approach.

Index Terms—Extended multiattribute profile (EMAP), flooding, joint sparsity-based model, landslide, multispectral (MS) satellite images, soil detection, synthetic spectral bands.

I. INTRODUCTION

ACCORDING to the United States Geological Survey (USGS) [1], landslides are a serious geological hazard in almost every state in the United States. It was estimated that they cause in excess of U.S. \$1 billion in damages and 25–50 deaths each year in the U.S. Globally, landslides cause billions in damages and thousands of deaths each year. Similarly, flooding also causes billions of dollars in damages in the U.S. [2]. In both cases, the soil may be exposed, which can be used as one of the indicators for damage assessment of landslides and flooding. In [3], we used multispectral (MS) images in the visible and near infrared (VNIR) range of Worldview-2 (WV-2) to detect soils that are related to excavated soils from illegal tunnel digging. There are two motivations for using satellite images for soil detection. First, satellites cover a large area, as compared to aircrafts. Second, as compared to Landsat (30-m resolution) and Moderate Resolution Imaging Spectroradiometer (500-m resolution), the WV-2 images have high enough spatial resolution to detect small bare-soil areas. In [3], we proposed a joint sparsity-based approach to soil detection where spatial, spectral, and feature domain information has been used. We observed that using 8-band MS images can yield much better detection performance than that of using only RGB bands.

M. Dao and C. Kwan are with Applied Research LLC., Rockville, MD 20850 USA (e-mail: ducminh174@gmail.com; chiman.kwan@arllc.net).

S. Bernabé is with the Department of Computer Science, Complutense University of Madrid, 28040 Madrid, Spain (e-mail: sebernab@ucm.es).

A. J. Plaza is with the Hyperspectral Computing Laboratory, Department of Technology of Computers and Communications, University of Extremadura, 10003 Cáceres, Spain (e-mail: aplaza@unex.es).

K. Koperski is with Digital Globe, Inc., Westminster, CO 80234 USA (e-mail: kkopersk@digitalglobe.com).

In this letter, we investigate how we can further improve the soil detection performance by using both original and synthetic bands. In particular, we explore the use of the extended multiattribute profile (EMAP) [4], which has been proven to significantly improve the land cover classification using MS images.

Once EMAPs are generated in our context, we apply a joint sparsity approach to both the original and EMAP bands. In particular, spatial- and spectral-domain characteristics are utilized in the joint sparsity approach. Extensive experiments show that soil detection performance can be further improved quite significantly.

There are two important contributions in our letter. First, this is an important preliminary study that uses MS satellite images to detect soil that may indicate the level of damage of landslides, flooding, and so on. Second, this is a followup work on illegal tunnel digging activity detection [3]. We integrated the EMAP with a joint sparsity approach that yielded unprecedented performance improvement in the soil detection.

The rest of this letter is organized as follows. Section II summarizes the data and the concept of EMAP, followed by a presentation of a joint sparsity-based approach to soil detection in Section III. Extensive experimental results are given in Section IV. Finally, a brief conclusion is provided in Section V.

II. DATA AND EMAP

A. Data Collection

Based on an earlier study [3] where known soils exist, we retrieved three WV-2 images (eight bands), near the border area between Tijuana and San Diego, collected on March 19, 2010, October 11, 2010, and December 2, 2010, containing new traces of soil that have been verified manually. Furthermore, some images also contain new soil vestiges of other activities (e.g., airport construction), which will be used as training samples for our detection algorithms.

B. Extended Multiattribute Profile

EMAP [4] is an extended idea of AP, a method that has recently been presented as an efficient tool for spectral–spatial analysis of remote sensing images [5]. APs provide a multilevel characterization of an image obtained by applying a sequence of morphological attribute filters to model different kinds of structural information on a single-band (or grayscale) image. These attribute filters can be morphological operators (the so-called features), such as thinning or thickening operators that process an image by merging its connected pixels. APs using different types of attribute features on different threshold levels can be stacked together, generating EMAPs [4].

Mathematically, given an input grayscale image f and a sequence of threshold levels $\{T_1, T_2, \ldots T_n\}$, the AP of f is
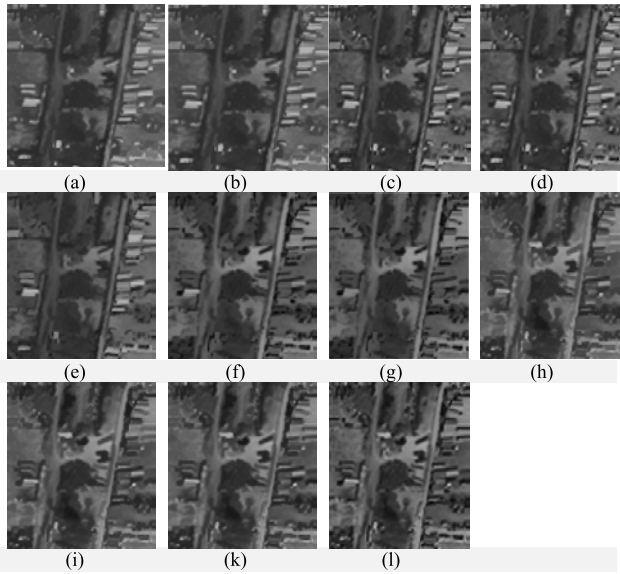
Fig. 1. Eleven output bands obtained after applying EMAP to the first band of an MS WV-2 image using thickening and thinning operators for "area" attribute at two threshold levels, and "diagonal" attribute at three threshold levels, respectively.
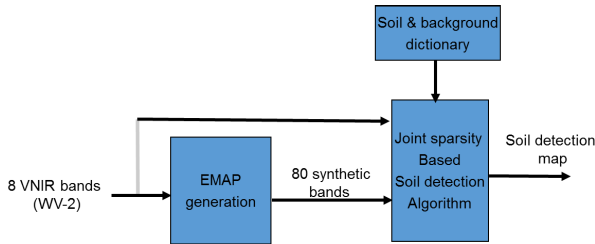

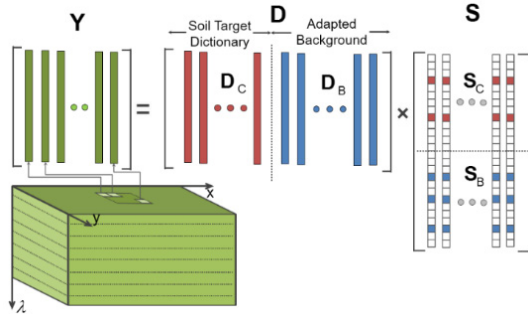Fig. 2. Proposed soil detection approach.

Fig. 3. Soil detection via a joint-sparsity model.

obtained by applying a sequence of thinning and thickening attribute transformations to every pixel in f

$$\mathrm{AP}(f) = \{\phi_1(f), \phi_2(f), \ldots \phi_n(f), f, \gamma_1(f), \gamma_2(f), \ldots \gamma_n(f)\} \quad (1)$$

where ϕ_i and γ_i ($i = 1, 2, \ldots, n$) are the thickening and thinning operators at threshold T_i, respectively. The EMAP of f is then acquired by stacking two or more APs using any feature reduction technique on MS/hyperspectral images, such as purely geometric attributes (e.g., area, length of the perimeter, image moments, and shape factors) or textural attributes (e.g., range, standard deviation, and entropy) [4]

$$\mathrm{EMAP}(f) = \{\mathrm{AP}_1(f), \mathrm{AP}_2(f) \ldots \mathrm{AP}_m(f)\}. \quad (2)$$

More details about EMAP can be found in [4]. Fig. 1 exhibits the 11 output bands obtained after applying
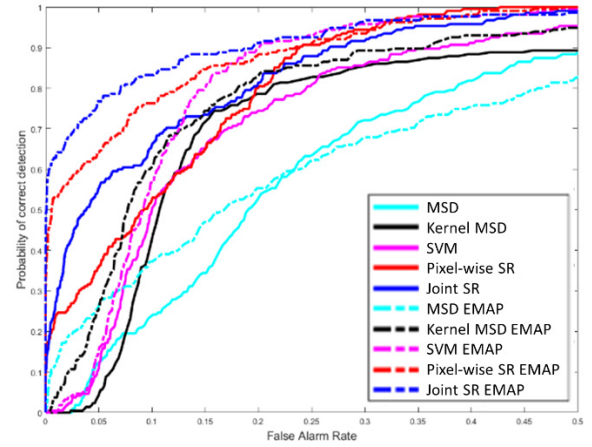

Fig. 4. Comparison of ROC curves of the results presented in Fig. 7(c)–(m) for both original and EMAP data. Image collected on March 19, 2010.
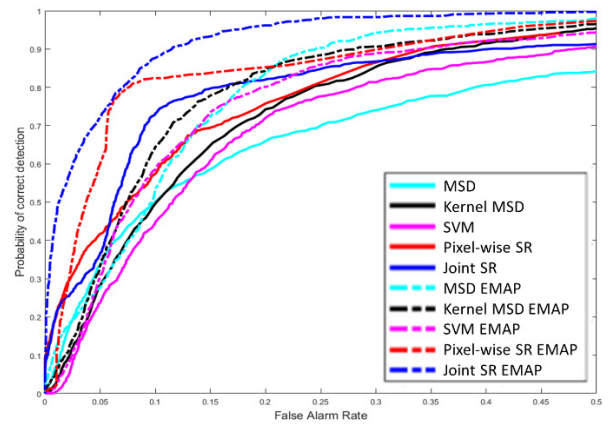

Fig. 5. Comparison of ROC curves of the results presented in Fig. 8(c)–(m) for both original and EMAP data. Image collected on November 11, 2010.
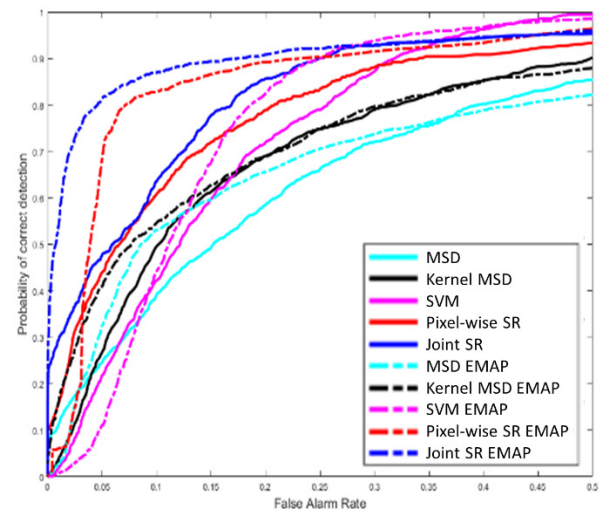

Fig. 6. Comparison of ROC curves of the results presented in Fig. 9(c)–(m) for both original and EMAP data. Image collected on December 2, 2010.

the EMAP for the first band of an MS image. Fig. 1(a) shows the original image; Fig. 1(b) and (c) shows the outputs by a thickening operator for the two threshold levels of "area" attribute at the sizes of 100 and 150 pixels, respectively; Fig. 1(d) and (e) shows the outputs by a thinning operator for the same two threshold levels of "area" attribute; Fig. 1(f)–(h) shows the outputs by a thickening operator for the three
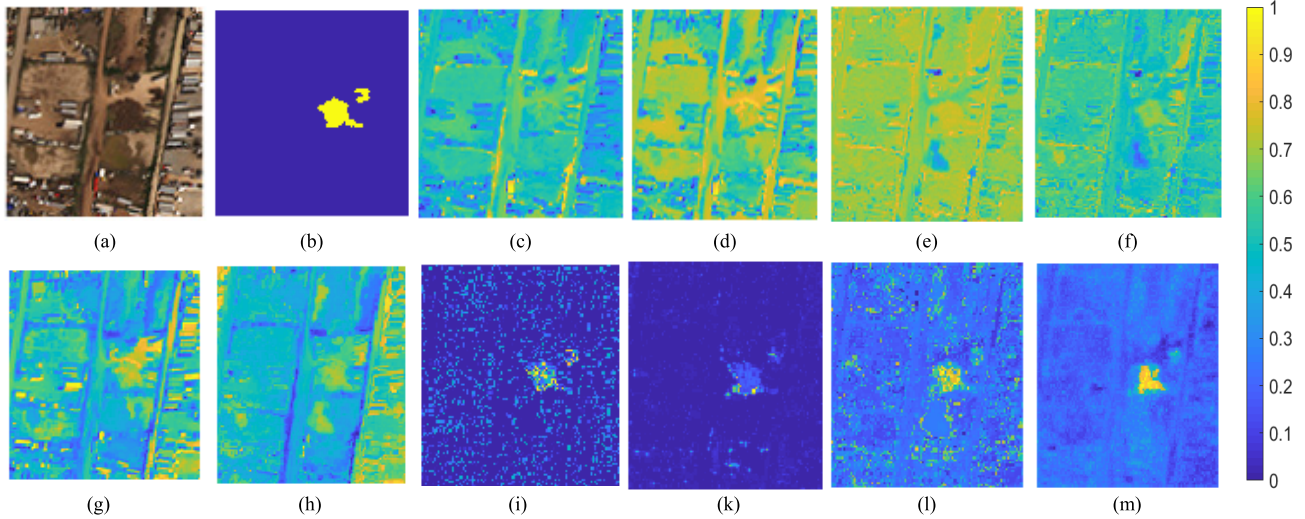
Fig. 7. Comparison of soil detection performance on a test area extracted from a MS image collected on March 19, 2010. (a) Original RGB image. (b) Manually selected target map (ground-truth). (c), (e), (g), (i), and (l) Soil detection performance via MSD, KerMSD, SVM, pixelwise SR, and JSR methods for original 8-band MS data, respectively. (d), (f), (h), (k), and (m) Soil detection performance via MSD, KerMSD, SVM, pixelwise SR, and JSR methods for extended 88-band EMAP data, respectively.

threshold levels of "diagonal" attribute with the diagonal lengths of the bounding box at 50, 100, and 500 pixels, respectively; and Fig. 1(i)–(l) shows the outputs by a thinning operator for the three same threshold levels of "diagonal" attribute.

III. SPARSITY-BASED APPROACH TO SOIL DETECTION

Our proposed soil detection approach can be summarized by using Fig. 2. The eight original VNIR bands in the WV-2 images are combined with 80 EMAP bands to form an 88-band data cube. A joint sparsity-based detection algorithm is then applied to detect soils. A dictionary of soil and background pixels is built offline using 88-band training data.

Small neighborhoods of pixels usually belong to the same class of materials. As such, we propose a joint sparsity model by gathering multiple pixels in small neighborhood areas and enforce them to have the same sparsity support of the signal representation over training samples. Fig. 3 illustrates our soil target detection model via joint sparse representation (JSR) [6]–[8]. Here, the input is an 88-band stacked data cube containing both the original bands and EMAP features.

Mathematically, let $Y = [y_1, y_2, \ldots, y_K] \in \mathbb{R}^{M \times K}$ be the columnwise concatenated measurement matrix of K neighboring pixels collected from a small patch such as a 3×3 or 5×5 patch, $D_C = [d_C^1, d_C^2, \ldots, d_C^{N_C}]$ and $D_B = [d_B^1, d_B^2, \ldots, d_B^{N_B}]$ contain the training samples of soil target and background, respectively, and contain the training samples of soil target and background, respectively, and $D = [D_C \ D_B] \in \mathbb{R}^{M \times N}$ (where $N = N_C + N_B$) be the combined target-background dictionary. The K pixels in a spatial neighborhood area can be compactly represented as

$$Y = [y_1, y_2, \ldots, y_K]$$
$$= [D_C \ D_B] \begin{bmatrix} S_C \\ S_B \end{bmatrix} = DS \quad (3)$$

where $S = [s^1, s^2, \ldots, s^K] \in \mathbb{R}^{N \times K}$ is the concatenation of the coefficient vectors of the corresponding K pixels. In the joint sparsity model, the sparse vectors $\{s^i\}_{i=1,2,\ldots,K}$ share the same sparse support and, thus, S is a sparse matrix with only a few nonzero rows. The joint sparsity structure for the soil target detection can be exploited by solving the following optimization problem:

$$\min_S \|Y - DS\|_F \quad \text{s.t.} \quad \|S\|_{\text{row},0} \leq s_0 \quad (4)$$

or it can be efficiently solved via a convex $l_{1,q}$-norm minimization problem

$$\min_S \|S\|_{1,q} \quad \text{s.t.} \quad Y = DS \quad (5)$$

where $\|S\|_{\text{row},0}$ is defined as the number of nonzero rows of S, s_0 denotes a predefined maximum row-sparsity level, $\|.\|_F$ is the Frobenious norm of a matrix, and $\|S\|_{1,q}$ with $q > 1$ is a norm defined as $\|S\|_{1,q} = \sum_{i=1}^N \|s_{i,:}\|_q$ with $s_{i,:}$s being rows of the matrix S, which encourages shared sparsity patterns across multiple observations.

The problem in (4) can be approximately solved by the simultaneous versions of the orthogonal matching pursuit (OMP) algorithm (simultaneous OMP or SOMP) [9] or subspace pursuit (SSP), while the $l_{1,q}$-norm row-sparse regularization in (5) can be solved via the alternating direction method of multipliers (ADMM) on the augmented Lagrangian multiplier function [10]. In this letter, we favor SOMP because of its fast and efficient computations. After the row-sparse matrix S is solved, the label of the center pixel in the neighboring area is then similarly determined to be either a soil or background sample by the minimal total residual rule, which selects the index of smaller residual with respect to the soil target or background dictionary, where the residual of the target dictionary is $r_C = \|Y - D_C S_C\|_F$, and the residual of the background dictionary is defined $r_B = \|Y - D_B S_B\|_F$.

IV. EXPERIMENTAL RESULTS

We conducted experiments for the new soil detection approach on both the original 8-band MS data and extended 88-band EMAP data using three test data sets collected on
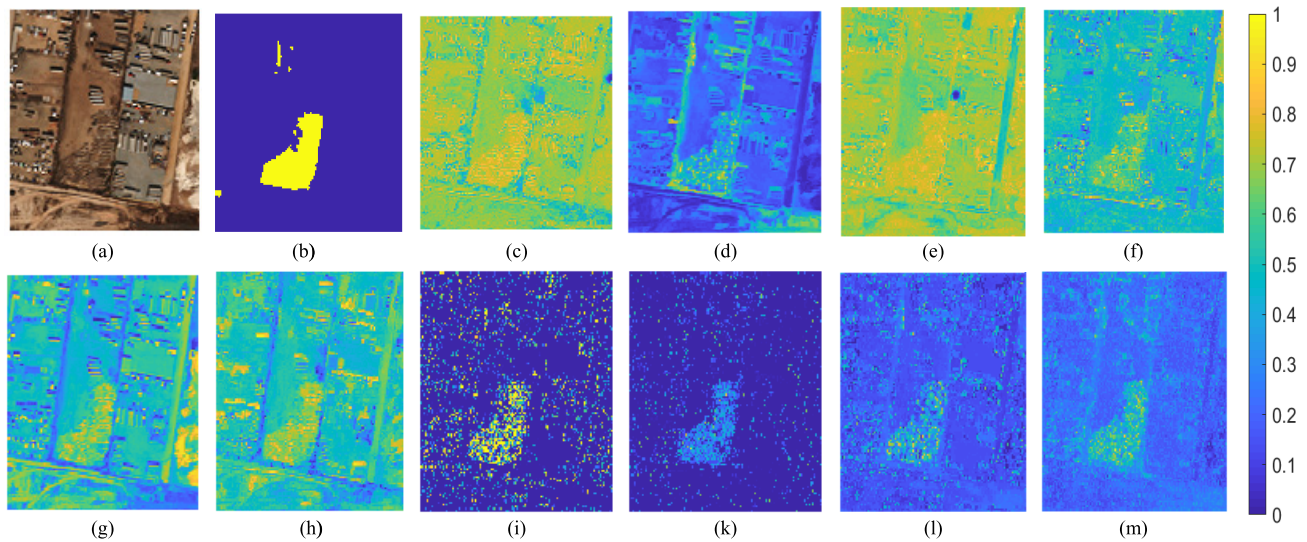
Fig. 8. Comparison of soil detection performance on a test area extracted from an MS image collected on October 11, 2010. (a) Original RGB image. (b) Manually selected target map (ground-truth). (c), (e), (g), (i), and (l) Soil detection performance via MSD, KerMSD, SVM, pixelwise SR and JSR methods for original 8-band MS data, respectively. (d), (f), (h), (k), and (m) Soil detection performance via MSD, KerMSD, SVM, pixelwise SR, and JSR methods for extended 88-band EMAP data, respectively.
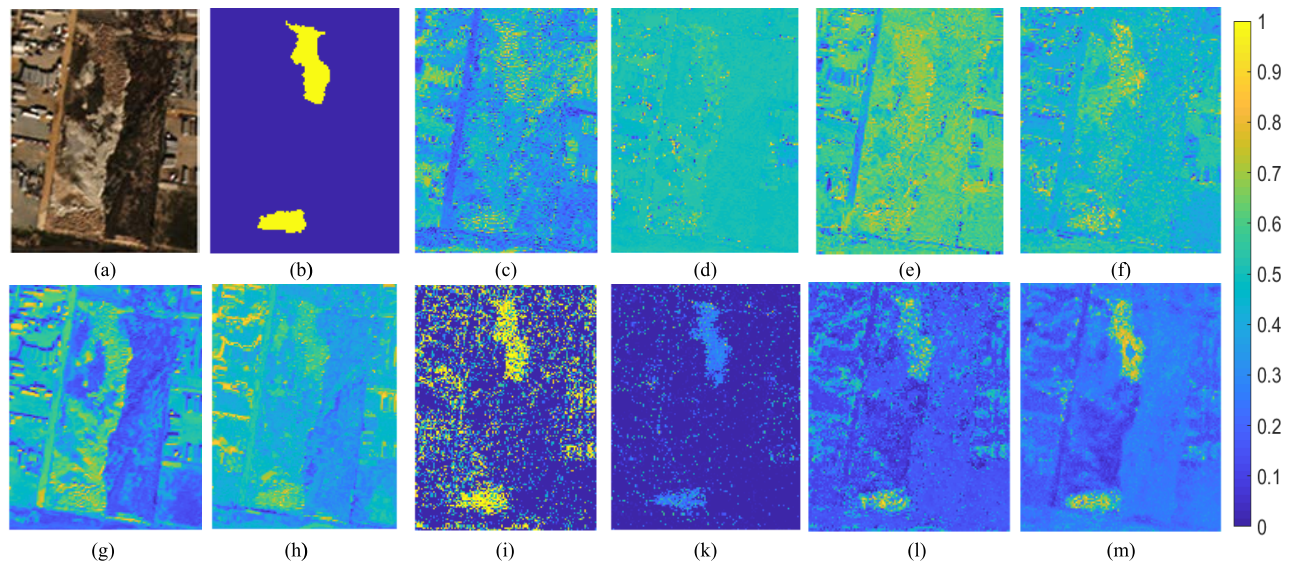
Fig. 9. Comparison of soil detection performance on a test area extracted from an MS image collected on December 2, 2010. (a) Original RGB image. (b) Manually selected target map (ground-truth). (c), (e), (g), (i), and (l) Soil detection performance via MSD, KerMSD, SVM, pixelwise SR, and JSR methods for original 8-band MS data, respectively. (d), (f), (h), (k), and (m) Soil detection performance via MSD, KerMSD, SVM, pixelwise SR, and JSR methods for extended 88-band EMAP data, respectively.

three different days: March 19, 2010, October 11, 2010, and December 2, 2010. Images were captured on the border area between Tijuana and San Diego where many illegal tunnel digging activities have been observed. In each test set, the ground truth was selected by visually inspecting and comparing the changes from different images captured during a short time frame (normally several days or weeks) up to pixel level. In all experiments, the soil target and background dictionary were constructed by randomly selecting 1000 samples from each soil-signature and background-signature training sets taken from different days and areas, respectively (i.e., $N_C = N_B = 1000$). For our joint-sparsity model, a 5×5 square neighborhood patch was used and the sparsity level is set to $s_0 = 5$. We used twofold-cross validation on the training samples to learn other parameters that give the best

results. Parameters in other methods have also been finetuned to obtain the best performance.

Figs. 4–6 shows the receiver operating characteristic (ROC) curves of all detection methods, including JSR [3], matched subspace detector (MSD) [11], kernel MSD (KerMSD) [12], support vector machine (SVM) [13], and pixelwise SR [14] methods, for both 8-band original data (displayed by solid lines) and 88-band EMAP data (displayed by dash lines). The ROC curves clearly demonstrate the improvement of detection performance on EMAP data in comparison to those on MS data. One example is shown in Fig. 5. At a 5% false alarm rate (FAR), the proposed joint sparsity approach with EMAP can reach close to 75% detection accuracy, whereas those methods without using EMAP can only reach less than 40% accuracy. Another example is shown in Fig. 6. At a 5%

TABLE I
COMPARISON OF DETECTION ACCURACIES ON MS AND EMAP DATA WITH FAR OF 10% ON THREE DIFFERENT
DAYS: MARCH 19, 2010, OCTOBER 11, 2010, AND DECEMBER 2, 2010

Method	03-19-2010		10-11-2010		12-02-2010	
	MS data	EMAP data	MS data	EMAP data	MS data	EMAP data
MSD	26.05	67.91	50.21	53.33	39.20	52.94
KerMSD	43.26	60.00	50.10	64.38	49.55	54.53
SVM	50.70	63.26	45.00	58.33	42.29	44.38
Pixel-wise SR	54.42	73.95	57.40	82.40	60.80	82.89
JSR	75.81	81.86	72.92	87.60	63.58	87.06

FAR, the proposed joint sparsity approach with EMAP can reach over 80% detection accuracy, whereas those methods without using EMAP can only reach less than 50% accuracy. Table I shows the comparison of the accurate detection rates of all models at the FARs of 10% for the three test sets. Some improvements are quite dramatic. For example, for data collected on December 2, 2010, the JSR detection accuracy with EMAP is 87.06%, which is 24% more than that obtained using the original 8-band data. The results of other detectors such as SVM also improved by 10%–40%. For instance, for March 19, 2010 data, the MSD performance has been improved from 26% to 68%. This clearly demonstrates the effectiveness of expanding spectral dimensionality using AP imposing spatial information on limited-spectral-resolution data. In each experimental set, the visualized detection results (exhibited in Figs. 7–9) on MS and EMAP data are compared using detection methods mentioned earlier. It can be seen that Fig. 7(m) displays the results of using the proposed approach, and Figs. 7–9 display very crisp detection results, as compared to results using other detectors. The visual comparisons shown in Figs. 7–9 further corroborate the objective performance metrics shown in Figs. 4–6.

V. CONCLUSION

We developed a new framework that incorporates jointly the spatial- and spectral-domain information using EMAP bands, derived from MS satellite images, for detecting anomalies and applied it to soil detection. Extensive studies demonstrated that the soil detection performance is very good in terms of ROC curves.

One potential future direction is to combine a sparsity-based approach with a deep learning-based approach [15] for soil detection. Another direction is to apply the proposed approach to fused Planet and WV images [16], which can provide higher temporal resolution, for change detection [17], [18]. A third direction is to integrate the proposed algorithm with damage assessment software for accurate detection of damages due to flooding, landslides, and so on. The fourth direction is to apply the proposed approach to illegal tunnel digging activity detection [3], [19]. Finally, we plan to investigate tent detection in refugee camps near the Syrian–Jordanian border using the proposed method here.

ACKNOWLEDGMENT

REFERENCES

[1] *USGS Landslide Website*. Accessed: Apr. 26, 2019. [Online]. Available: https://landslides.usgs.gov/learn/ls101.php

[2] *Flood Damage in the US*. Accessed: Apr. 26, 2019. [Online]. Available: http://www.flooddamagedata.org/national.html

[3] M. Dao, C. Kwan, K. Koperski, and G. Marchisio, "A joint sparsity approach to tunnel activity monitoring using high resolution satellite images," in *Proc. IEEE Ubiquitous Comput., Electron. Mobile Commun. Conf.*, New York, NY, USA, Oct. 2017, pp. 322–328.

[4] S. Bernabé, P. R. Marpu, A. Plaza, M. D. Mura, and J. A. Benediktsson, "Spectral–spatial classification of multispectral images using kernel feature space representation," *IEEE Geosci. Remote Sens. Lett.*, vol. 11, no. 1, pp. 288–292, Jan. 2014.

[5] M. Dalla Mura, J. A. Benediktsson, B. Waske, and L. Bruzzone, "Morphological attribute profiles for the analysis of very high resolution images," *IEEE Trans. Geosci. Remote Sens.*, vol. 48, no. 10, pp. 3747–3762, Oct. 2010.

[6] M. Dao, C. Kwan, B. Ayhan, and T. D. Tran, "Burn scar detection using cloudy MODIS images via low-rank and sparsity-based models," in *Proc. IEEE Global Conf. Signal Inf. Process.*, Washington, DC, USA, Dec. 2016, pp. 177–181.

[7] S. Li, W. Wang, H. Qi, B. Ayhan, C. Kwan, and S. Vance, "Low-rank tensor decomposition based anomaly detection for hyperspectral imagery," in *Proc. IEEE Int. Conf. Image Process. (ICIP)*, Quebec City, QC, Canada, Sep. 2015, pp. 4525–4529.

[8] W. Wang, S. Li, H. Qi, B. Ayhan, C. Kwan, and S. Vance, "Identify anomaly componentbysparsity and low rank," in *Proc. IEEE Workshop Hyperspectral Image and Signal Process., Evol. Remote Sensor (WHIS-PERS)*, Tokyo, Japan, Jun. 2015, pp. 1–4.

[9] J. A. Tropp, A. C. Gilbert, and M. J. Strauss, "Algorithms for simultaneous sparse approximation. Part I: Greedy pursuit," *Signal Process.*, vol. 86, no. 3, pp. 572–588, 2006.

[10] S. Boyd, N. Parikh, E. Chu, B. Peleato, and J. Eckstein, "Distributed optimization and statistical learning via the alternating direction method of multipliers," *Found. Trends Mach. Learn.*, vol. 3, no. 1, pp. 1–122, 2011.

[11] D. Manolakis, C. Siracusa, and G. Shaw, "Adaptive matched subspace detectors for hyperspectral imaging applications," in *Proc. Int. Conf. Acoust., Speech Signal Process.*, vol. 5, 2001, pp. 3153–3156.

[12] H. Kwon and N. M. Nasrabadi, "Kernel matched subspace detectors for hyperspectral target detection," *IEEE Trans. Pattern Anal. Mach. Intell.*, vol. 28, no. 2, pp. 178–194, Feb. 2006.

[13] F. Melgani and L. Bruzzone, "Classification of hyperspectral remote sensing images with support vector machines," *IEEE Trans. Geosci. Remote Sens.*, vol. 42, no. 8, pp. 1778–1790, Aug. 2004.

[14] M. Dao, D. Nguyen, T. Tran, and S. Chin, "Chemical plume detection in hyperspectral imagery via joint sparse representation," in *Proc. Military Commun. Conf. (MILCOM)*, 2012, pp. 1–5.

[15] D. Perez *et al.*, "Deep learning for effective detection of excavated soil related to illegal tunnel activities," in *Proc. IEEE Ubiquitous Comput., Electron. Mobile Commun. Conf.*, New York, NY, USA, Oct. 2017, pp. 626–632.

[16] C. Kwan *et al.*, "Assessment of spatiotemporal fusion algorithms for planet and worldview images," *Sensors*, vol. 18, no. 4, p. 1051, Mar. 2018.

[17] C. Kwan, "Remote sensing performance enhancement in hyperspectral images," *Sensors*, vol. 18, no. 11, p. 3598, 2018.

[18] J. Zhou, C. Kwan, B. Ayhan, and M. T. Eismann, "A novel cluster kernel RX algorithm for anomaly and change detection using hyperspectral images," *IEEE Trans. Geosci. Remote Sens.*, vol. 54, no. 11, pp. 6497–6504, Nov. 2016.

[19] Y. Lu, D. Perez, M. Dao, C. Kwan, and J. Li, "Deep learning with synthetic hyperspectral images for improved soil detection in multispectral imagery," in *Proc. IEEE Ubiquitous Comput., Electron. Mobile Commun. Conf.*, New York, NY, USA, Nov. 2018, pp. 1–8.